



## Investigation of depth-resolved nanoscale structural changes in regulated cell proliferation and chromatin decondensation

Title	Investigation of depth-resolved nanoscale structural changes in regulated cell proliferation and chromatin decondensation
Author(s)	Uttam, Shikhar;Bista, Rajan K.;Staton, Kevin;Alexandrov, Sergey;Choi, Serah;Bakkenist, Christopher J.;Hartman, Douglas J.;Brand, Randall E.;Liu, Yang
Publication Date	2013
Repository DOI	<a href="https://doi.org/10.1364/BOE.4.000596">10.1364/BOE.4.000596</a>

# Investigation of depth-resolved nanoscale structural changes in regulated cell proliferation and chromatin decondensation

Shikhar Uttam,<sup>1,\*</sup> Rajan K. Bista,<sup>1</sup> Kevin Staton,<sup>1</sup> Sergey Alexandrov,<sup>2</sup> Serah Choi,<sup>3</sup> Christopher J. Bakkenist,<sup>3</sup> Douglas J. Hartman,<sup>4</sup> Randall E. Brand,<sup>5</sup> and Yang Liu<sup>1</sup>

<sup>1</sup>Biomedical and Optical Imaging Laboratory (BOIL), Departments of Medicine and Bioengineering, University of Pittsburgh, Pittsburgh, PA 15213, USA

<sup>2</sup>Tissue Optics and Microcirculation Imaging Group (TOMI), School of Physics, National University of Ireland, Galway, Ireland

<sup>3</sup>Department of Radiation Oncology, University of Pittsburgh School of Medicine, Pittsburgh, PA 15232, USA

<sup>4</sup>Department of Pathology, School of Medicine, University of Pittsburgh, Pittsburgh, PA 15213, USA

<sup>5</sup>Department of Medicine, University of Pittsburgh, Pittsburgh, PA 15213, USA

\*shf28@pitt.edu

**Abstract:** We present depth-resolved spatial-domain low-coherence quantitative phase microscopy, a simple approach that utilizes coherence gating to construct a depth-resolved structural feature vector quantifying sub-resolution axial structural changes at different optical depths within the sample. We show that this feature vector is independent of sample thickness variation, and identifies nanoscale structural changes in clinically prepared samples. We present numerical simulations and experimental validation to demonstrate the feasibility of the approach. We also perform experiments using unstained cells to investigate the nanoscale structural changes in regulated cell proliferation through cell cycle and chromatin decondensation induced by histone acetylation.

©2013 Optical Society of America

**OCIS codes:** (180.3170) Interference microscopy; (300.6300) Spectroscopy, Fourier transforms; (170.4730) Optical pathology; (170.1610) Clinical applications.

---

## References and links

1. S. Iyer, R. M. Gaikwad, V. Subba-Rao, C. D. Woodworth, and I. Sokolov, "Atomic force microscopy detects differences in the surface brush of normal and cancerous cells," *Nat. Nanotechnol.* **4**(6), 389–393 (2009).
2. H. Knecht and S. Mai, "3D imaging of telomeres and nuclear architecture: an emerging tool of 3D nano-morphology-based diagnosis," *J. Cell. Physiol.* **226**(4), 859–867 (2011).
3. H. Subramanian, P. Pradhan, Y. Liu, I. R. Capoglu, X. Li, J. D. Rogers, A. Heifetz, D. Kunte, H. K. Roy, A. Taflove, and V. Backman, "Optical methodology for detecting histologically unapparent nanoscale consequences of genetic alterations in biological cells," *Proc. Natl. Acad. Sci. U.S.A.* **105**(51), 20118–20123 (2008).
4. H. Subramanian, H. K. Roy, P. Pradhan, M. J. Goldberg, J. Muldoon, R. E. Brand, C. Sturgis, T. Hensing, D. Ray, A. Bogojevic, J. Mohammed, J. S. Chang, and V. Backman, "Nanoscale cellular changes in field carcinogenesis detected by partial wave spectroscopy," *Cancer Res.* **69**(13), 5357–5363 (2009).
5. R. K. Bista, T. A. Brentnall, M. P. Bronner, C. J. Langmead, R. E. Brand, and Y. Liu, "Using optical markers of nondysplastic rectal epithelial cells to identify patients with ulcerative colitis-associated neoplasia," *Inflamm. Bowel Dis.* **17**(12), 2427–2435 (2011).
6. K. J. Chalut, J. H. Ostrander, M. G. Giacomelli, and A. Wax, "Light scattering measurements of subcellular structure provide noninvasive early detection of chemotherapy-induced apoptosis," *Cancer Res.* **69**(3), 1199–1204 (2009).
7. I. Itzkan, L. Qiu, H. Fang, M. M. Zaman, E. Vitkin, I. C. Ghiran, S. Salahuddin, M. Modell, C. Andersson, L. M. Kimerer, P. B. Cipolloni, K. H. Lim, S. D. Freedman, I. Bigio, B. P. Sachs, E. B. Hanlon, and L. T. Perelman, "Confocal light absorption and scattering spectroscopic microscopy monitors organelles in live cells with no exogenous labels," *Proc. Natl. Acad. Sci. U.S.A.* **104**(44), 17255–17260 (2007).
8. Z. Wang, K. Tangella, A. Balla, and G. Popescu, "Tissue refractive index as marker of disease," *J. Biomed. Opt.* **16**(11), 116017 (2011).
9. G. Popescu, *Quantitative Phase Imaging of Cells and Tissues*, McGraw-Hill biophotonics (McGraw-Hill, 2011), pp. xx, 362 p.

10. N. N. Boustany, S. A. Boppart, and V. Backman, "Microscopic imaging and spectroscopy with scattered light," *Annu. Rev. Biomed. Eng.* **12**(1), 285–314 (2010).
11. H. K. Roy, H. Subramanian, D. Damania, T. A. Hensing, W. N. Rom, H. I. Pass, D. Ray, J. D. Rogers, A. Bogojevic, M. Shah, T. Kuzniar, P. Pradhan, and V. Backman, "Optical detection of buccal epithelial nanoarchitectural alterations in patients harboring lung cancer: implications for screening," *Cancer Res.* **70**(20), 7748–7754 (2010).
12. P. Wang, R. Bista, R. Bhargava, R. E. Brand, and Y. Liu, "Spatial-domain low-coherence quantitative phase microscopy for cancer diagnosis," *Opt. Lett.* **35**(17), 2840–2842 (2010).
13. P. Wang, R. K. Bista, W. E. Khalbuss, W. Qiu, S. Uttam, K. Staton, L. Zhang, T. A. Brentnall, R. E. Brand, and Y. Liu, "Nanoscale nuclear architecture for cancer diagnosis beyond pathology via spatial-domain low-coherence quantitative phase microscopy," *J. Biomed. Opt.* **15**(6), 066028 (2010).
14. R. K. Bista, S. Uttam, D. J. Hartman, W. Qiu, J. Yu, L. Zhang, R. E. Brand, and Y. Liu, "Investigation of nuclear nano-morphology marker as a biomarker for cancer risk assessment using a mouse model," *J. Biomed. Opt.* **17**(6), 066014 (2012).
15. R. K. Bista, P. Wang, R. Bhargava, S. Uttam, D. J. Hartman, R. E. Brand, and Y. Liu, "Nuclear nano-morphology markers of histologically normal cells detect the "field effect" of breast cancer," *Breast Cancer Res. Treat.* **135**(1), 115–124 (2012).
16. T. Akkin, C. Joo, and J. F. de Boer, "Depth-resolved measurement of transient structural changes during action potential propagation," *Biophys. J.* **93**(4), 1347–1353 (2007).
17. C. Joo and J. F. de Boer, "Spectral-domain optical coherence reflectometric sensor for highly sensitive molecular detection," *Opt. Lett.* **32**(16), 2426–2428 (2007).
18. M. A. Choma, A. K. Ellerbee, C. Yang, T. L. Creazzo, and J. A. Izatt, "Spectral-domain phase microscopy," *Opt. Lett.* **30**(10), 1162–1164 (2005).
19. A. K. Ellerbee, T. L. Creazzo, and J. A. Izatt, "Investigating nanoscale cellular dynamics with cross-sectional spectral domain phase microscopy," *Opt. Express* **15**(13), 8115–8124 (2007).
20. C. Joo, C. L. Evans, T. Stepinac, T. Hasan, and J. F. de Boer, "Diffusive and directional intracellular dynamics measured by field-based dynamic light scattering," *Opt. Express* **18**(3), 2858–2871 (2010).
21. Y. Liu, X. Li, Y. L. Kim, and V. Backman, "Elastic backscattering spectroscopic microscopy," *Opt. Lett.* **30**(18), 2445–2447 (2005).
22. A. F. Fercher, C. K. Hitzenberger, G. Kamp, and S. Y. Elzaiat, "Measurement of intraocular distances by backscattering spectral interferometry," *Opt. Commun.* **117**(1-2), 43–48 (1995).
23. M. Born and E. Wolf, *Principles of Optics: Electromagnetic Theory of Propagation, Interference and Diffraction of Light*, 7th (expanded) ed. (Cambridge University Press, 1999).
24. X. J. Liang, A. Q. Liu, C. S. Lim, T. C. Ayi, and P. H. Yap, "Determining refractive index of single living cell using an integrated microchip," *Sens. Actuators A Phys.* **133**(2), 349–354 (2007).
25. L. Cherkezyan, H. Subramanian, V. Stoyneva, J. D. Rogers, S. Yang, D. Damania, A. Taflove, and V. Backman, "Targeted alteration of real and imaginary refractive index of biological cells by histological staining," *Opt. Lett.* **37**(10), 1601–1603 (2012).
26. D. J. Cook, *Cellular Pathology: Introduction to Techniques and Applications*, 2nd ed. (Scion, 2006), pp. xxxii, 384 p.
27. G. C. Crossman, "Mounting media for phase microscope specimens," *Stain Technol.* **24**(4), 241–247 (1949).
28. X. Li, A. Taflove, and V. Backman, "Recent progress in exact and reduced-order modeling of light-scattering properties of complex structures," *IEEE J. Sel. Top. Quantum Electron.* **11**(4), 759–765 (2005).
29. B. E. A. Saleh and M. C. Teich, *Fundamentals of Photonics*, 2nd ed., Wiley series in pure and applied optics (Wiley-Interscience, 2007), pp. xix, 1177 p.
30. D. Marchion and P. Münster, "Development of histone deacetylase inhibitors for cancer treatment," *Expert Rev. Anticancer Ther.* **7**(4), 583–598 (2007).
31. K. F. Tóth, T. A. Knoch, M. Wachsmuth, M. Frank-Stöhr, M. Stöhr, C. P. Bacher, G. Müller, and K. Rippe, "Trichostatin A-induced histone acetylation causes decondensation of interphase chromatin," *J. Cell Sci.* **117**(18), 4277–4287 (2004).
32. R. K. Bista, S. Uttam, P. Wang, K. Staton, S. Choi, C. J. Bakkenist, D. J. Hartman, R. E. Brand, and Y. Liu, "Quantification of nanoscale nuclear refractive index changes during the cell cycle," *J. Biomed. Opt.* **16**(7), 070503 (2011).
33. O. Momčilović, S. Choi, S. Varum, C. Bakkenist, G. Schatten, and C. Navara, "Ionizing radiation induces ataxia telangiectasia mutated-dependent checkpoint signaling and G(2) but not G(1) cell cycle arrest in pluripotent human embryonic stem cells," *Stem Cells* **27**(8), 1822–1835 (2009).

---

## 1. Introduction

The ability to identify structural changes in cells and tissue, especially at the nanometer scale during disease processes (e.g., cell differentiation, proliferation, gene expression, malignant transformation) has important implications in biomedical research and clinical diagnosis. Cellular nanoscale structural properties have received increasing attention as promising markers for pre-cancerous and cancerous cells [1–10]. Recent studies suggest that nanoscale

structural changes occur early in carcinogenesis and precede microscopically detectable cytological abnormalities. The analysis of nanoscale structural properties has shown great promise in early diagnosis and cancer risk assessment for different types of cancers [4,5,11]. Towards this end, we have developed an interferometric technique – spatial-domain low-coherence quantitative phase microscopy (SL-QPM) – that has shown potential to detect malignancy at a higher sensitivity than conventional pathology [12,13], and to quantify cancer risk [14,15].

SL-QPM uses a reflection-mode common-path low-coherence interferometric setup equipped with a broadband light source and spectroscopic detection. It quantifies changes in the optical path length (OPL), with nanoscale sensitivity, to capture the sub-resolution structural changes within the cell nucleus. The OPL is obtained by measuring the phase of the Fourier-transformed spectral interference signal at a specific optical depth of interest. The reflection-mode common-path setup suppresses the common-mode phase noise, while the spatial low-coherence of the light source prevents back-scattered light from one location within the sample from coherently combining with back-scattered light from another displaced location, resulting in the suppression of coherence-dependent speckle noise. A broadband light source is used for improved axial resolution.

Similar interferometric phase microscopy techniques have been successfully used to measure transient structural changes in nerve cells [16], perform real-time molecular detection [17], and measure cellular dynamics [18–20]. These techniques detect the sub-resolution change in OPL at a specific depth of interest corresponding to a distinct physical interface of interest with a strong refractive-index mismatch within the sample. As noted in these works, the implicit coherence gating allows the rejection of contributions to phase from locations outside the coherence length. Although these techniques have proven to be very valuable in tracking dynamic structural changes, their use in analyzing the nanoscale structural properties of static clinical specimens at different disease stages has been limited. If phase microscopy can be used to reliably analyze nanoscale cellular structural properties directly on clinically prepared human cell (cytology) or tissue (histology) samples, it could have significant implications in both basic understanding of structural alterations during disease processes and clinical disease diagnosis. According to the standard clinical protocol, cells or tissue are first fixed (e.g., using formalin), and then embedded in paraffin to prepare the cell or tissue block. For structural analysis, thin sections – a few microns thick – are cut from a cell or tissue block using a microtome, mounted on a microscope slide, deparaffinized and finally cover-slipped using a mounting medium. One of the biggest challenges in using phase microscopy for structural analysis of such clinically-prepared cell and tissue samples is decoupling the variation in section thickness from the actual structural changes within the cell or tissue.

In this paper we present a simple approach that builds upon SL-QPM to provide depth-resolved quantification of internal structural changes within the cell nucleus with regulated cell proliferation and chromatin decondensation – directly using clinically prepared unstained cell samples – where the structural changes associated with these biological processes are decoupled from those due to sample thickness variations. Both, depth-resolved quantification and removal of the effect of thickness variation are achieved by exploiting the coherence gating implicit in the spectral-domain interferometry. The resulting thickness-independent depth-resolved structural feature vector captures the sub-resolution structural changes at different, but *fixed* sample depths inside the sample.

We utilize SL-QPM optical-setup to implement the proposed approach. The underlying theory is presented in the following section. Numerical simulations are presented in Sections 3 through 5, where we show the independence of the depth-resolved structural feature vector from variation in sample thickness, study the effect of noise on the feature vector, and illustrate why our approach has the ability to capture depth-resolved structural changes. In Section 6, we first experimentally validate the use of implicit coherence gating to obtain the depth-resolved structural features that are independent of section thickness. Then using

clinically prepared cell blocks, we investigate the depth-resolved nanoscale structural alterations within the cell nucleus during the regulation of cell proliferation through cell cycle and chromatin decondensation induced by histone acetylation with altered chromatin density and structure. These experiments suggest that our depth-resolved approach has direct applicability in analyzing samples prepared using standard clinical protocol, and provide new insights into the structural transformation of cell nuclei during cell proliferation and chromatin decondensation. We present our conclusions in Section 7.

## 2. Depth-resolved structural characterization

The experimental setup of SL-QPM has been described in detail in our previous publications [12,14,21]. In brief, a collimated broadband light from Xenon-arc lamp is focused onto the sample by an objective (NA = 0.4). The sample itself forms a reflection-mode low-coherence common-path interferometry configuration. The reference and back-scattered waves from the sample are collected and projected by a tube lens onto the slit of an imaging spectrograph coupled to the CCD camera mounted on a scanning stage. The temporal coherence length of the system is  $1.225\mu\text{m}$  and the probing depth of the system is estimated to be  $79\mu\text{m}$ .

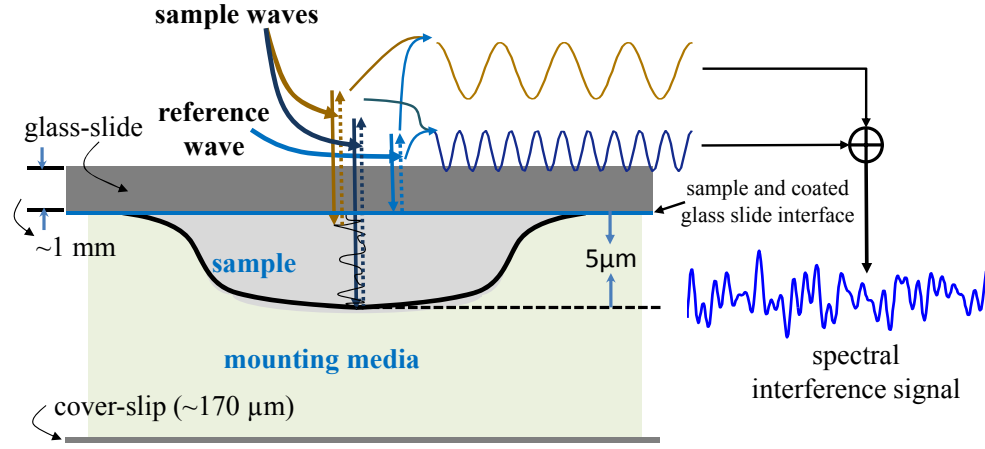


Fig. 1. The reflection-mode common-path interferometry setup based on clinically prepared glass slide. The setup dimensions and the axial refractive index profile have been exaggerated for clarity.

The sample consists of an unstained cell section with  $5\mu\text{m}$  thickness obtained by sectioning a paraffin-embedded cell block with a microtome, mounted on a coated glass-slide (80T/20R), and then cover-slipped using mounting medium with a refractive index of 1.50, as sketched in Fig. 1. The coated glass-slide on the top of the sample is approximately a millimeter thick. However, due to the small depth of field ( $\sim 4\mu\text{m}$ ) and limited probing depth of our system, when the incident light is focused onto the sample, the reference wave is generated by the reflection at the sample and the coated glass-slide interface. The reference wave is enhanced by the reflection coating on the glass slide. As the refractive index mismatch between the sample and the mounting medium is small, the sample wave consisting of backscattered waves from the heterogeneous components inside the scattering sample is not dominated by the reflection from the sample-mounting medium interface. The detected spectral signal can be written as

$$P(k) = S(k) \left[ r_r^2 + \int_0^z r_s^2(z') dz' + 2 \int_0^z r_s(z') r_r \cos(2kn(z')z') dz' \right], \quad (1)$$

where  $S(k)$  is the power spectrum of the source,  $r_r$  is the reflection coefficient of the sample and the coated glass-slide interface,  $r_s(z)$  is the scattering coefficient of the sample at depth  $z$ ,  $Z$  is the total sample thickness,  $n(z)$  is the refractive index distribution along the axial  $z$ -direction and  $k = 2\pi/\lambda$  is the wavenumber, with  $\lambda$  being the wavelength.

In the context of spectral-domain interferometry, Fercher et al. [22] showed that under the Born approximation [23] and the far-field assumption, the 3D spatial frequency corresponding to a monochromatic wave, after being scattered from the object of interest, is given by  $\mathbf{K} = (\mathbf{k}_s - \mathbf{k}_i)/2\pi$ . For the incident wave at normal illumination and collection, the back-scattered components are restricted to the axial  $z$ -direction, and the spatial frequency reduces to  $\mathbf{K} = (k/\pi) \mathbf{z}$ , where  $\mathbf{z}$  is the unit vector in the positive  $z$ -direction in frequency space. We can, therefore, re-write Eq. (1) as

$$P(\mathbf{K}) = S\left(\frac{\mathbf{K}}{2}\right) \left[ R_r + R_s + 2 \int_0^Z r_s(z') r_r \cos\left(4\pi \frac{\mathbf{K}}{2} n(z') z'\right) dz' \right], \quad (2)$$

where  $R_r = r_r^2$  and  $R_s = \int_0^Z r_s^2(z') dz'$ . The Fourier inverse of Eq. (2) results in

$$p(z_{\text{opl}}) = 2\Gamma \otimes \left[ (R_r + R_s) \delta(0) + 2r_r \mathcal{F}^{-1} \left( \int_0^Z r_s(z') \cos\left(4\pi \frac{\mathbf{K}}{2} n(z') z'\right) dz' \right) \right] (2z_{\text{opl}}), \quad (3)$$

which is a convolution of the source correlation function with the superposition of the reference wave and the backscattered sample wave. As a result, the amplitude and the phase of the Fourier-transformed signal at any given optical depth of interest has contributions only from the back-scattered waves within the coherence length around the given optical depth of interest. Choma et al. [18] showed that the phase of the Fourier transform of the spectral signal with respect to a fixed optical-depth location captures the sub-resolution change in OPL at that location. We calculate this sub-resolution change in OPL using the equation,

$$\delta p(z_{\text{opl}}) = \frac{\lambda_0}{2 \cdot 2\pi} \arctan \left( \frac{\text{Im}(p(z_{\text{opl}}))}{\text{Re}(p(z_{\text{opl}}))} \right), \quad (4)$$

where  $z_{\text{opl}}$  is the fixed optical depth location, and Im and Re denote the imaginary and real parts of the complex convolution  $p(z_{\text{opl}})$  respectively. Note that the factor of 2 accounts for the double OPL due to the reflection configuration.

For spectral-domain interferometry approaches reported in the literature, the implicit coherence gating has been used to extract the value of  $\delta p$  at a peak location that corresponds to a distinct physical interface of interest (due to a strong refractive index mismatch within the sample). In contrast to this traditional approach, we instead exploit the implicit coherence gating by obtaining  $\delta p$  at fixed optical depths within the samples that have small refractive index gradient (no strong interfaces), thereby removing the effect of sample thickness (as detailed in Section 3). The fixed optical depth locations are chosen such that the distance between them is at least one coherence length of the correlation function. Figure 2 illustrates this approach. A representative spectral interference signal from a given scattering object for an ideal light source with nearly infinite bandwidth is shown in Fig. 2(i). The corresponding OPL profile, obtained by Fourier transforming this spectral interference signal, represents the true OPL profile of the scattering object, and is depicted by the distinct blue stem-plot in Fig. 2(ii). However, due to the limited spectral bandwidth of the light source, only a limited range of the spatial frequencies from the scattering object are captured, as visualized through the

windowing function in Fig. 2(i). As a result, the Fourier relation between spatial frequency and OPL manifests as a convolution between the source correlation function (i.e., Fourier transform of the power spectral density of the source) and the actual OPL profile of the scattering object derived from an ideal light source with nearly infinite bandwidth. The resulting coherence gating implicit in this convolution is illustrated in Fig. 2(ii). The final OPL profile using a light source with a limited bandwidth is shown in Fig. 2(iii), with the original distinct peaks in the true OPL profile significantly broadened.

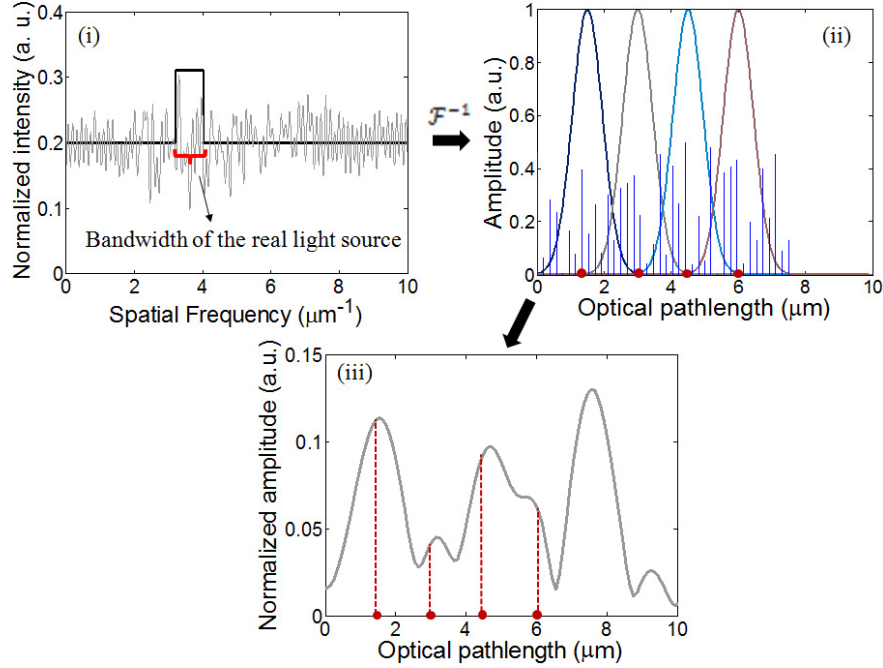


Fig. 2. Illustration of depth-resolved SL-QPM via coherence gating at fixed depth locations (shown as red dots).

Note that in clinically prepared samples, there is no predominant physical interface with a significant refractive index mismatch. As a result, the OPL profile has contributions from the backscattering signals from all depths within the sample, and does not exhibit a dominant peak corresponding to a specific physical interface. Therefore, for clinically prepared samples, instead of identifying structural changes at any specific physical interface, a more cogent strategy is to identify structural changes at fixed optical-depth locations in such a way that the source correlation functions around these optical depths cover the axial sample depth-range of interest. Towards this end, we first fix the optical-depth locations such that they are separated by at least one coherence length. As a result, the  $\delta p$  value at each of these locations (indicated by the red dots in Figs. 2(ii)-(iii)) captures the internal structural change within the coherence-gated optical section around each optical depth. Next, depending on the sample thickness (see the following section), a sufficient number of optical depth-locations are chosen to ensure that the entire sample depth-range of interest is covered. The  $\delta p$  values from these optical-depth locations then form the elements of a depth-resolved feature vector that characterizes the sub-resolution structural alterations within the sample. Note that due to the coherence-length separation, the elements of the structural feature vector – the  $\delta p$  values – are independent of each other. A necessary condition for the depth-resolved feature vector to be valid is that the signal strength at the selected locations is above the noise floor. In Section 4 we show that our system satisfies this condition.

### 3. Effect of sample thickness

The actual sample thickness for a specified value is controlled by the precision of the microtome, a tool commonly used to section the sample into thin slices of specified thickness for clinical cell or tissue specimens. Due to imperfect precision in microtome sectioning, some variation in the thickness of the sectioned sample is inevitable, as shown in Fig. 3. It plots a representative thickness profile of a sample section measured using Dektak profilometer, which has a resolution of  $5\text{\AA}$ . If the location corresponding to the physical interface at the sample and mounting medium (within the OPL profile) is used, the measured  $\delta p$  at this interface will significantly depend on the variation in sample thickness. However, if a fixed optical depth location inside the sample is chosen such that the variation in section thickness of the sample is outside the coherence length around this chosen location, then  $\delta p$  at this fixed optical depth location, and all the other preceding locations, will not be affected by the variations in sample thickness. Using ten samples we have empirically determined that the maximum deviation in sample thickness from the chosen section thickness of  $5\mu\text{m}$  is less than  $500\text{nm}$ , as visually exemplified in Fig. 3.

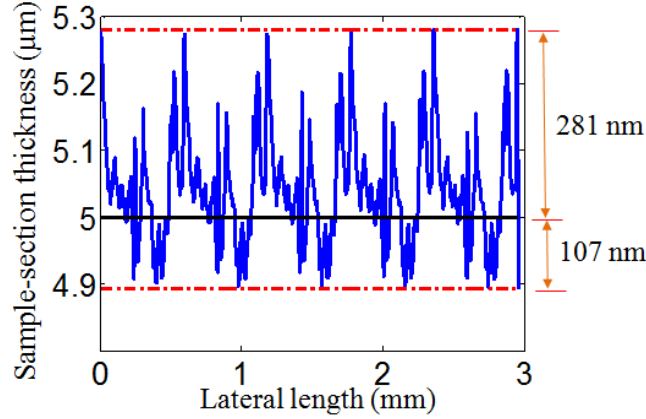


Fig. 3. A representative sample thickness profile of a tissue sectioned using a microtome.

With this experimentally determined bound on sample thickness variation, we perform numerical simulation to illustrate the independence of the depth-resolved structural feature vector from sample thickness. As shown in Fig. 4, we construct a one-dimensional (1D) axial refractive index profile  $n(z)$  with  $5\mu\text{m}$  sample thickness with a step-size of  $25\text{ nm}$ . This profile is generated using a Gaussian random field (GRF). Each value of  $n(z)$  is a Gaussian random variable with mean  $n_0 = \langle n(z) \rangle$  and standard deviation  $\langle \Delta n \rangle = \sqrt{\langle [n(z) - n_0]^2 \rangle}$ . The angular brackets denote the ensemble expectation. The Gaussian function is used as the two-point correlation function:  $C_n(z) = \exp(-z^2 / (l_c / 2)^2)$ , where  $l_c$  is the spatial correlation length of refractive index representing the length scale over which the spatial correlation decreases to a negligible level. The model parameters are chosen to be consistent with the specifications of the experimental condition. Specifically, the average refractive index of the fixed tissue section  $n_0$  is assumed to be  $1.53$  (note that the dehydrated cells and tissue are reported to have a refractive index of  $1.50$  to  $1.55$  [12,24–27]), with the standard deviation  $\langle \Delta n \rangle$  and the correlation length  $l_c$  of the spatial variation of refractive index being  $0.002$  and  $50\text{nm}$ , respectively. This 1D profile has been previously used to model the refractive index profile of biological samples, in accordance with available literature [3,28]. Following the common-mode reflection configuration sketched in Fig. 1, the reflection from the sample and the glass-slide interface acts as the reference wave. The refractive index of the glass-slide

is assumed to be 1.515. Collimated light from a broadband source (498nm – 625nm) is

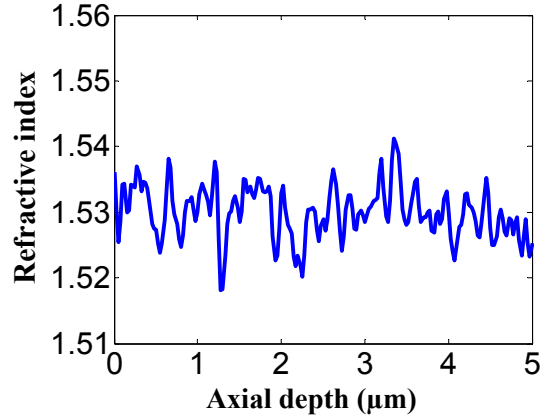


Fig. 4. A representative axial refractive index profile of the scattering sample.

normally incident on the modeled scattering object, and the spectral-domain interference signal resulting from the superposition of the reference and the back-scattered waves is collected. The back-scattered waves from the sample are generated by modeling the axial refractive index profile as a layered media, and by using the wave-transfer matrix and scattering matrix formalism to describe the reflection from within the sample [29].

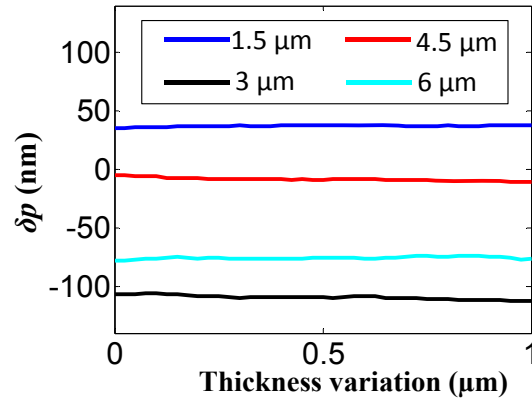


Fig. 5. Variation in  $\delta p$  as a function of variation in sample thickness.

For the broadband light source considered, and using the relationship between spatial frequency, wave-vector, and wavelength explained in Section 2, the spatial-frequency bandwidth is  $0.816 \text{ lp}/\mu\text{m}$  with the resulting coherence length being  $1.225\mu\text{m}$ . We, therefore, use the fixed optical-depth locations of  $1.5\mu\text{m}$ ,  $3\mu\text{m}$ ,  $4.5\mu\text{m}$ , and  $6\mu\text{m}$ , which, for a mean refractive index of 1.53, correspond to the physical-depth locations of  $0.98\mu\text{m}$ ,  $1.96\mu\text{m}$ ,  $2.94\mu\text{m}$ , and  $3.92\mu\text{m}$  respectively. The average physical thickness of the scattering sample is  $5\mu\text{m}$ , corresponding to the mean optical thickness of  $7.65\mu\text{m}$ . A variation in sample thickness of  $\pm 500\text{nm}$  translates into the change in optical thickness of  $\pm 765\text{nm}$ . Consequently, the optical thickness of the sample varies between  $6.8850\mu\text{m}$  and  $8.4150\mu\text{m}$ . Due to the coherence gating, the sub-resolution structural change in OPL,  $\delta p$ , at the optical depth location of  $6\mu\text{m}$  carries the structural information of the scattering sample from the depth

range of  $6 \pm 0.6125\mu\text{m}$ , which lies well outside the variation in optical thickness of the sample ( $6.8850 - 8.4150\mu\text{m}$ ). We, therefore, expect that this variation will not affect the  $\delta p$  values at the fixed optical-depth locations of  $1.5\mu\text{m}$ ,  $3\mu\text{m}$ ,  $4.5\mu\text{m}$ , and  $6\mu\text{m}$ . This expectation is confirmed by our simulation results. Figure 5 shows that  $\delta p$  values remain stable – with maximum deviation of  $2\text{nm}$  – for the four optical-depth locations as the sample-section thickness changes from  $4.5\mu\text{m}$  to  $5.5\mu\text{m}$ .

#### 4. Effect of noise

The use of depth-resolved feature-vector to characterize structural change requires that the  $\delta p$  values for the four optical-depth locations are not affected by noise, that is, there is no variation in  $\delta p$  values over repeated measurements of the same sample. This requirement is essential to ensure consistent and repeatable performance without adversely affecting the system sensitivity. Toward this end we present simulation-based stability performance of feature-vector measurements as a function of SNR for shot-noise limited detection. For this type of detection, the noise photons per detector are,

$$N_{noise} = \sqrt{\frac{\eta P_{ref} \tau}{h\nu} \frac{2}{N}}, \quad (5)$$

where,  $\eta$  is the quantum efficiency of the detector,  $\tau$  is acquisition time,  $h\nu$  is the photon quantum energy, and  $N$  is the number of detectors. The signal photons per detector are,

$$N_{Signal} = \frac{2\eta \sqrt{P_{sig} P_{ref}} \tau}{h\nu} \frac{2}{N}. \quad (6)$$

Accounting for the fact that Fourier transform results in the coherent integration of the signal and the incoherent integration of noise, the system SNR is,

$$\text{SNR} = 10 \log_{10} \frac{4\eta P_{sig} \tau}{h\nu} \frac{2}{N} \text{ dB}. \quad (7)$$

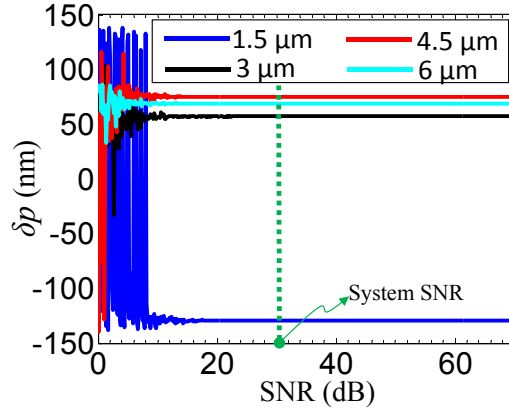


Fig. 6. The sub-resolution in change in OPL ( $\delta p$ ) as a function of SNR for the same refractive index profile at fixed optical-depth locations of  $1.5\mu\text{m}$ ,  $3\mu\text{m}$ ,  $4.5\mu\text{m}$  and  $6\mu\text{m}$ .

For our simulation we consider a fixed refractive index profile that is used to generate the  $\delta p$  values at the four optical-depth locations for changing SNR. The simulation is performed using the method outlined in Section 3. Shot noise, which follows Poisson

statistics, is simulated through a Gaussian process with white spectrum, whose mean is zero, and standard deviation is proportional to  $\sqrt{P_{ref}}$ . Under experimental conditions, with sufficiently large number of photons collected by the detector, it is reasonable to simulate Poisson distribution through a Gaussian distribution. Figure 6 shows the  $\delta p$  values at the four optical-depth locations for changing SNR. As can be seen, for low SNR all four  $\delta p$  values fluctuate wildly. However, as SNR increases the values converge to a stable value, with variation in  $\delta p$  of less than  $\pm 0.1\text{nm}$  for SNR greater than 22 dB. In the figure we have also indicated the SNR of 31 dB for our system, which is well within the stable region.

Apart from the system SNR, the presence of a distinct interface (strong refractive index mismatch) along the refractive index profile has the potential to adversely affect the  $\delta p$  values at different depth locations despite the coherence gating. The coherence gating is implemented implicitly by performing a Fourier transform. The resulting correlation function that serves as the coherence gate does not taper-off smoothly, but instead has side lobes (even after using smoothing windows such as the Hanning window). Consequently, the energy from a strong reflected wave can leak into the correlation functions at different depths, thereby affecting the  $\delta p$  values at those depths. Figure 7 illustrates this scenario. It shows the  $\delta p$  value at the optical depth location of  $1.5\mu\text{m}$  for changing refractive index mismatch that occurs at the optical depth location of  $6.5\mu\text{m}$ . The mismatch is quantified as a multiple ( $m$ ) of the standard deviation  $\langle \Delta n \rangle$  of the refractive index profile. As can be seen, for a large mismatch of more than three times  $\langle \Delta n \rangle$ , the energy from the strong refractive index mismatch leaks into the correlation function at  $1.5\mu\text{m}$ , affecting its  $\delta p$  value. Therefore, our approach is only applicable to samples whose refractive index profile does not have very strong refractive index mismatch.

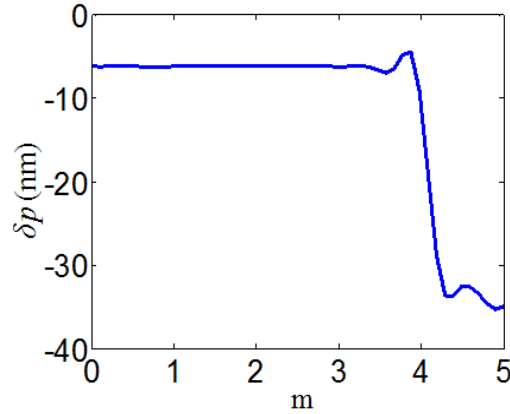


Fig. 7. The sub-resolution in change in OPL ( $\delta p$ ) at optical depth location of  $1.5\mu\text{m}$  as a function of refractive index mismatch at the optical depth of  $6.5\mu\text{m}$ , quantified by  $m < \Delta n >$ .

## 5. Contribution of structural characteristics to $\delta p$

As shown in Eq. (2) in reference [18], the depth-resolved  $\delta p$  values capture the sub-resolution change in OPL at the specified optical-depth locations. This sub-resolution change in OPL quantifies the structural change within the coherence-gated optical section around each of the fixed optical-depth locations. To exemplify this concept, we perform the numerical simulation using the GRF model presented in Section 3 to investigate the effect of two statistical parameters that characterize the structural properties of the sample: the average magnitude of the local mean refractive index  $\delta n$ , and the local spatial correlation length of refractive index

profile  $l_c$ . The former characterizes the change in local density of macromolecules, while the latter is a statistical measure of the spatial scale of the refractive-index variation (e.g., the presence of larger macromolecules increases  $l_c$ ). Using these two parameters, we simulate the conditions that individually isolate the effects of  $\delta n$  and  $l_c$  on the measured sub-resolution structural change. Figure 8 shows the effect of local change in mean refractive index of the axial refractive index profile that was generated from a GRF model with a fixed correlation length. As shown in Fig. 8(i), the mean refractive index within the region delineated by red rectangular-box – physical depth range of  $2.5\mu\text{m}$  to  $3.5\mu\text{m}$  approximately corresponding to the optical depth range of  $3.9\mu\text{m}$  to  $5.3\mu\text{m}$  – is varied from 0 to 0.01.

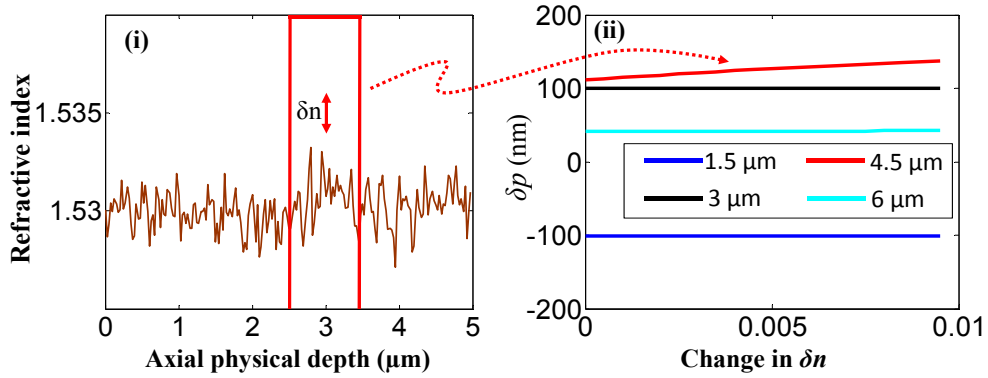


Fig. 8. The relationship between  $\delta p$  and changes in local mean refractive index ( $\delta n$ ).

Figure 8(ii) shows that this change in local mean refractive index is captured by  $\delta p$  values at the fixed optical depth location of  $4.5\mu\text{m}$ . Next, keeping the local mean refractive index constant, and changing the local spatial correlation length of the axial refractive index profile within the same region as the previous example, we observe that  $\delta p$  also captures the change in  $l_c$ . This is shown in Fig. 9, where the change in  $l_c$  is again detected at the  $4.5\mu\text{m}$  optical-depth location. Combining the above two results we observe that to a first approximation  $\delta p \propto \delta n l_c$ .

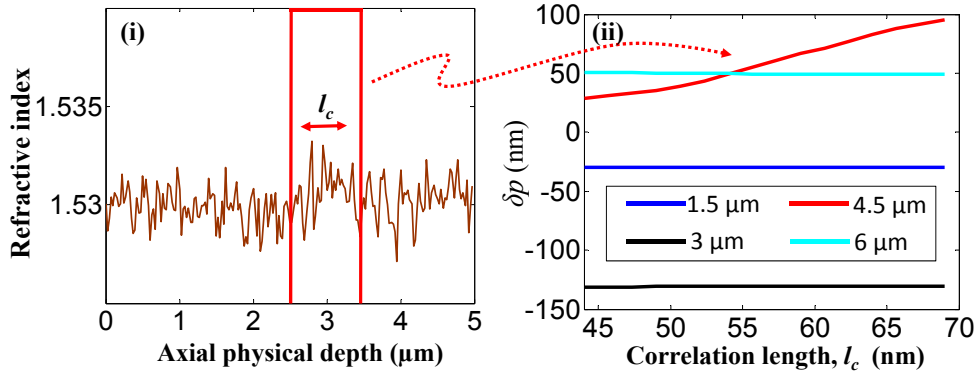


Fig. 9. Relationship between  $\delta p$  and the profile correlation length,  $\delta l$  (nm).

We next present two scenarios to illustrate the feasibility of depth-resolved feature vector to capture sub-resolution nanoscale structural changes at different sample depths. Figure 10(i) shows the first example where a significant change in mean refractive index occurs in the

sample-section ranging from  $0.5\mu\text{m}$  to  $1.5\mu\text{m}$ , and Fig. 10(ii) shows an example where the mean refractive index primarily changes within the range of  $2.5\mu\text{m}$  to  $3.5\mu\text{m}$ . For the first scenario four hundred refractive index profiles are generated using the GRF model with the same  $\delta n$  and  $l_c$  to represent the complexity present in biological samples. Two hundred of these profiles (exemplified by the blue refractive index profile in Fig. 10(i)) are considered as is, while for the remaining two hundred profiles an average offset of  $0.005$  is added to  $\delta n$  within the sample-section ranging from  $0.5\mu\text{m}$  to  $1.5\mu\text{m}$  (red refractive index profile in Fig. 10(i)). The same steps are followed to realize the second scenario, except that now, as shown in Fig. 10(ii), the average offset is added to the sample-section ranging from  $2.5\mu\text{m}$  to  $3.5\mu\text{m}$ . Figures 10(iii) and 10(iv) show the corresponding calculated  $\delta p$  values for the two scenarios at the four fixed optical-depth locations of  $1.5\mu\text{m}$ ,  $3\mu\text{m}$ ,  $4.5\mu\text{m}$ , and  $6\mu\text{m}$ . For each refractive index profile, the  $\delta p$  values at the specified locations result in a depth-resolved structural feature vector. As can be seen in Figs. 10(iii) and 10(iv), the change in mean refractive index  $\delta n$  within the sample depth range of  $0.5\mu\text{m}$  to  $1.5\mu\text{m}$  and depth range of  $2.5\mu\text{m}$  to  $3.5\mu\text{m}$  is captured at the corresponding optical depth location of  $1.5\mu\text{m}$  and  $4.5\mu\text{m}$ , respectively. Thus, due to the depth-resolved nature of the measured  $\delta p$  values, the structural feature-vector components are well-separated at the specified fixed optical depths where the structural changes occur. For the rest of the optical depths with the same local mean refractive index  $\delta n$ , the structural feature-vector components overlap.

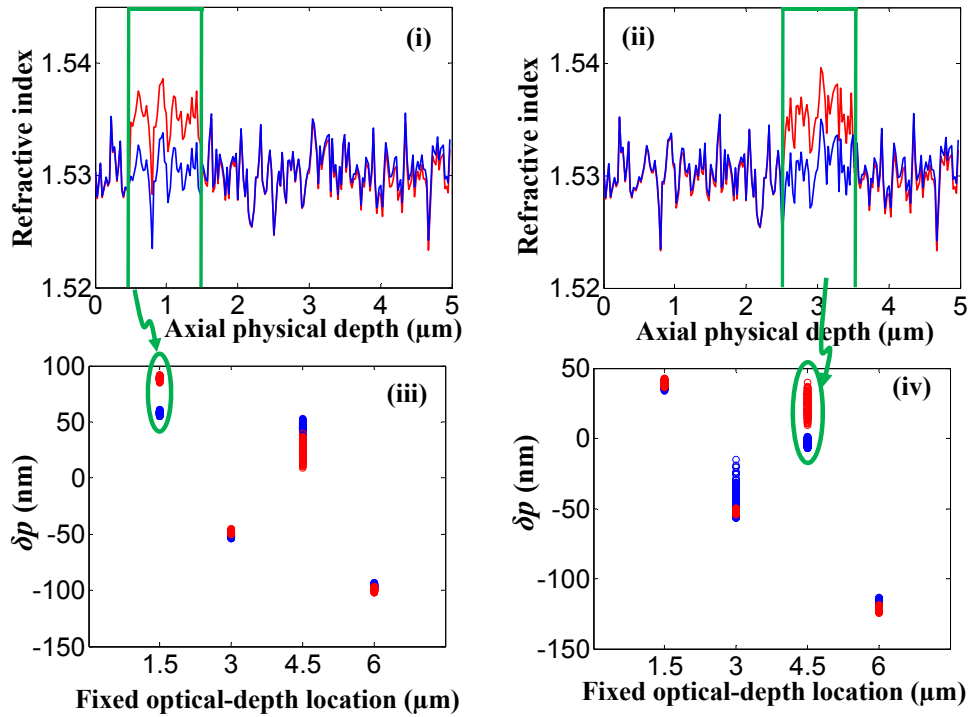


Fig. 10. The depth-resolved sub-resolution change in OPL ( $\delta p$ ).

## 6. Experimental results

### 6.1 Experimental demonstration of coherence gating

We have numerically shown that implicit coherence gating can be employed to obtain a depth-resolved structural feature vector that captures the sub-resolution structural changes at

different, but fixed sample depths inside the sample, independent of section thickness. We now present experimental results that validate the use of implicit coherence gating.

We used serial tissue sections of the small intestinal tissue from a normal mouse sectioned at two different thicknesses –  $4\mu\text{m}$  and  $5\mu\text{m}$  – using a microtome, placed on the coated glass slide, coverslipped with a mounting medium ( $n = 1.50$ ), without any staining. As the tissue sections are serial sections of the same tissue segment, it is reasonable to assume that these two tissue sections have similar structural properties, but different thickness. With the SL-QPM instrument, we analyzed the spectral interference signal for each  $(x,y)$  pixel location from a similar tissue area – expressed as a function of spatial frequency  $\mathbf{K}$ . We Fourier-transformed the spectral signal to get the axial OPL profile of the sample at  $(x,y)$  location from which, using Eq. (4), we then extracted  $\delta p(x,y,z_{opl})$  at  $z_{opl} = 1.5\mu\text{m}$  and  $3\mu\text{m}$ . Our claim, based on the simulation results, is that the implicit coherence gating should ensure that the  $\delta p$  values measured at the two optical depth locations inside the tissue section should not be affected by the section thickness. Figures 11(i) and 11(ii) show the  $\delta p$  values for  $4\mu\text{m}$  and  $5\mu\text{m}$  thick sections at optical depths of  $1.5\mu\text{m}$  and  $3\mu\text{m}$  respectively. This result clearly shows that the  $\delta p$  values at the two optical depths are independent of the section thickness.

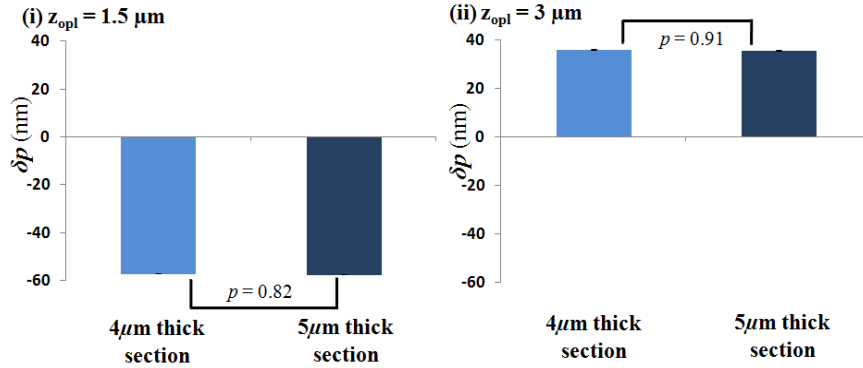


Fig. 11. The depth-resolved sub-resolution change in OPL ( $\delta p$ ) for  $4\mu\text{m}$  and  $5\mu\text{m}$  thick sections at fixed optical-depth locations within the tissue section of (i)  $1.5\mu\text{m}$  and (ii)  $3\mu\text{m}$  respectively.

## 6.2 System stability

We investigated the temporal stability of the depth-resolved  $\delta p$  values at the fixed optical depth locations of  $1.5\mu\text{m}$ ,  $3\mu\text{m}$ ,  $4.5\mu\text{m}$ , and  $6\mu\text{m}$  by plotting them as a function of time. The result is shown in Fig. 12. As can be seen these depth-resolved values are relatively stable with a standard deviation from the mean value of around 1nm. Specifically, the standard deviation due to temporal fluctuations in  $\delta p$  values at the optical depth locations of  $1.5\mu\text{m}$ ,  $3\mu\text{m}$ ,  $4.5\mu\text{m}$ , and  $6\mu\text{m}$  is 0.76nm, 0.78nm, 0.86nm and 1.2nm respectively. The measurements were made on a phantom consisting of a monolayer of  $0.75\mu\text{m}$  polystyrene microspheres sandwiched between two  $2\mu\text{m}$  thick paraffin layers. The system SNR was 33 dB.

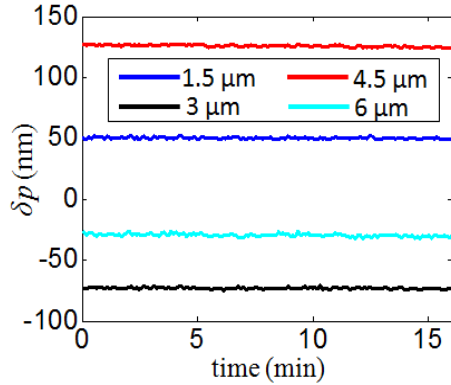


Fig. 12. Temporal stability of depth-resolved  $\delta p$  values as a function of time at four fixed optical depth locations.

### 6.3 Experiments with biological cells

As we showed in Section 5, there are two major structural characteristics that can change the structural feature vector: the mean refractive index  $\delta n$  associated with the macromolecular density, and the spatial correlation length of refractive index  $l_c$  associated with the spatial scale of macromolecular structures. We investigate two important cancer-related biological processes in which an immortalized cancer cell line is treated with drugs that induce changes in these two types of structural characteristics as proof-of-concept demonstration. In the first experiment detailed in Section 6.3.1, the cell proliferation and division process is modulated by thymidine and nocodazole during cell cycle to double the DNA content in the cell nucleus and increase the nuclear density and refractive index ( $\delta n$ ). In the second experiment presented in Section 6.3.2, we investigate the structural changes as a result of histone acetylation, induced by Trichostatin A (TSA), a histone deacetylase (HDAC) inhibitor. The histone acetylation is a well-known epigenetic change to control the gene activity [30]. It has previously been shown using transmission electron microscopy [30] and confocal microscopy [31] that there is a subsequent local relaxation of chromatin or chromatin decondensation, which is expected to increase the chromatin structural correlation length ( $l_c$ ).

#### 6.3.1 Regulation of cell proliferation

We first analyzed the nuclear structural changes in HeLa cells in response to drugs that modulate the cell proliferation. Cells are first treated with double-thymidine, which inhibits the DNA synthesis and arrest cells at  $G_1/S$  phase; and then treated with nocodazole, which prevents cell division to arrest cells at  $G_2/M$  phase, resulting in doubled DNA content in the cell nucleus and thus higher nuclear density and refractive index. Such cell synchronization process also populates most cells at a distinct phase, thus reducing the heterogeneity in the cell population in each phase.

HeLa cells were grown in Dulbecco's Modified Eagle Medium (DMEM) supplemented with 10% fetal bovine serum (FBS) (Mediatech, Inc) and 1% penicillin-streptomycin in a 70% humidified incubator at 37°C and 5%  $CO_2$ . Cells were treated using a previously described protocol [32] based on double-thymidine block followed by nocodazole. As confirmed by flow cytometry result shown in Fig. 13, 81% of the cells are arrested at  $G_1/S$  phase and 70% of the cells are arrested at  $G_2/M$  phase. The DNA content of the nucleus at the  $G_2/M$  phase is indeed double that of the cells at  $G_1/S$  phase. Next we prepared a cell block [32] to mimic the clinical sample preparation, which is then sectioned at 5  $\mu m$ . The cell-block section is placed on a coated glass slide (80T/20R), de-paraffinized and coverslipped with a mounting medium ( $n = 1.50$ ), without any staining.

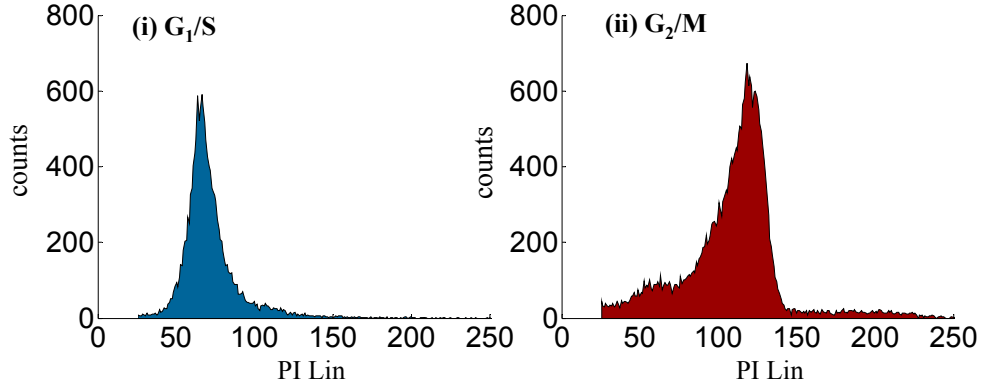


Fig. 13. Flow cytometry of HeLa cells arrested at (i)  $G_1/S$ -phase (ii)  $G_2/M$ -phase.

The cell nuclei can be easily identified in the bright-field image. With the SL-QPM instrument, for each  $(x,y)$  pixel location within the cell nuclei, we obtained the spectral signal as a function of spatial frequency  $\mathbf{K}$ . The Fourier-transform of the spectral signal gave us the axial OPL profile of the sample at the  $(x,y)$  location. Figure 14 shows an example of a measured spectral signal  $I(x,y,\lambda)$  from a cell nucleus (Fig. 14(i)) and its Fourier transform after removing the bias term (Fig. 14(ii)). Using Eq. (4) we then extracted  $\delta p(x,y,z_{opt})$  from the axial OPL profile at optical depths of  $1.5\mu\text{m}$ ,  $3\mu\text{m}$ ,  $4.5\mu\text{m}$  and  $6\mu\text{m}$ . The resulting depth-resolved structural feature vectors for all  $(x,y)$  pixel locations were averaged over the pixel locations within the cell nucleus to generate a mean depth-resolved structural feature vector for every cell nucleus. We analyzed 90 cell nuclei for each phase.

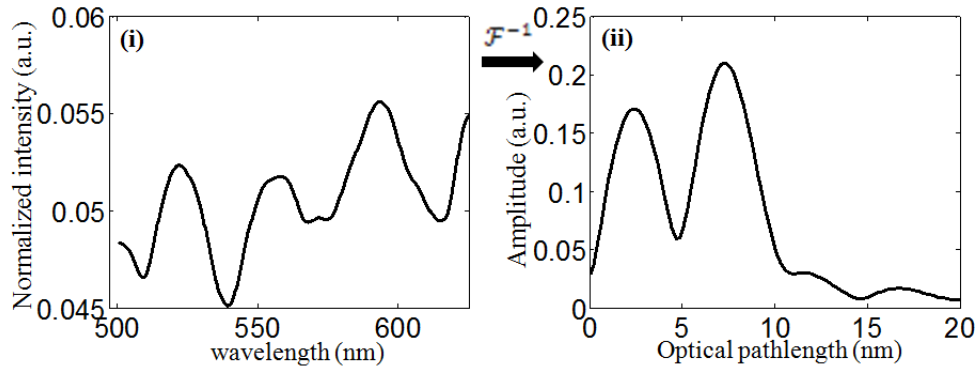


Fig. 14. Spectral signal from a cell nucleus and its Fourier transform.

Figure 15 shows the comparison of  $\delta p$  at optical-depth locations of  $1.5\mu\text{m}$ ,  $3\mu\text{m}$ ,  $4.5\mu\text{m}$  and  $6\mu\text{m}$  within the cell nuclei for cells at  $G_1/S$  and  $G_2/M$  phases. Overall, a significant increase in the average  $\delta p$  is seen at three out of four optical depths ( $1.5$ ,  $3$  and  $4.5\mu\text{m}$ ) within cell nuclei at  $G_2/M$  phase compared to those at  $G_1/S$  phase. The doubled DNA content at  $G_2/M$  phase increases the nuclear density and refractive index ( $\delta n$ ), resulting in a higher  $\delta p$ . In particular, the depth-resolved  $\delta p$  shows that the most statistically significant change is observed at the optical depth location of  $3\mu\text{m}$ , which approximately corresponds to the middle part of the cell nucleus. The depth-resolved average nuclear structural change between cells at  $G_2/M$  and  $G_1/S$  phases, quantified by  $\delta(\delta p) = \delta p_{G_2/M} - \delta p_{G_1/S}$ , is presented in Fig. 16 for graphic visualization. It shows a heterogeneous distribution of altered nuclear density at

different optical-depth locations, with the most significant changes occurring at the center of the cell nuclei (indicated by the darker areas in Fig. 16) for this sample set.

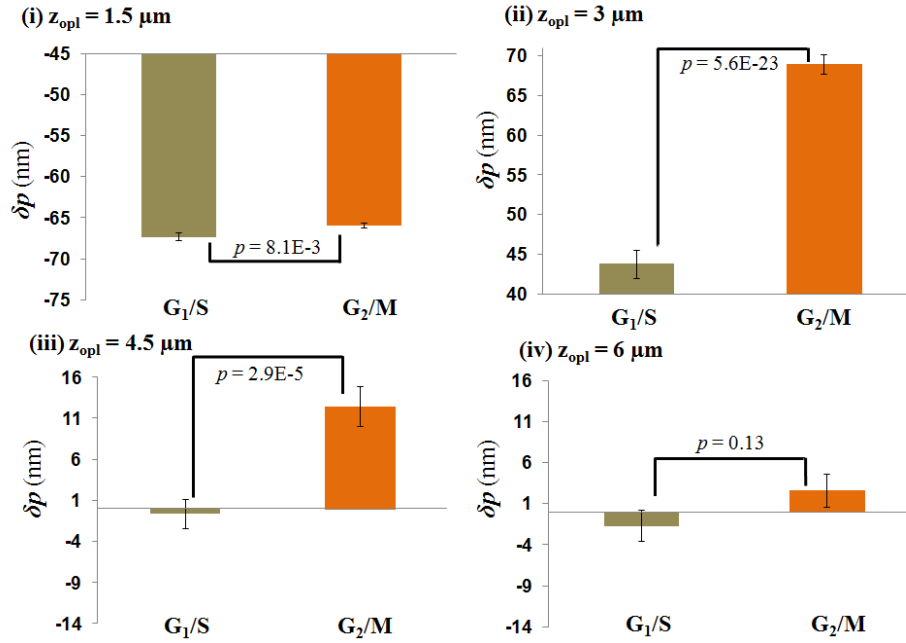


Fig. 15. The depth-resolved sub-resolution change in OPL ( $\delta p$ ) at four fixed optical-depth locations within the nuclei for cells at G<sub>1</sub>/S and G<sub>2</sub>/M phase. The two-sided p-value is shown on each figure, calculated from the student *t*-test.

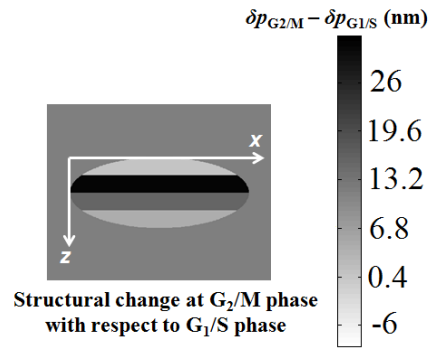


Fig. 16. The depth-resolved distribution of altered nuclear density in cells at G<sub>2</sub>/M phase compared to those at G<sub>1</sub>/S phase. The gray scale bar shows the change in  $\delta p$  for G<sub>2</sub>/M with respect to that of G<sub>1</sub>/S phase.

### 6.3.2 Histone acetylation

We also investigated the depth-resolved structural change in cells following histone acetylation, which are treated with TSA, a histone deacetylase inhibitor that induces chromatin decondensation. Chromatin decondensation was anticipated to be associated with a more “loosened” chromatin conformation [30] and an increased correlation length was therefore anticipated. Asynchronous HeLa cells were treated with either 1 μM DMSO (vehicle) or 1 μM TSA in DMSO for 6 h (Fig. 17, lanes 1 and 2 left). HeLa cells were also synchronized using the double-thymidine block protocol described in Section 6.1 with the single modification that 1 μM DMSO or 1 μM TSA in DMSO were added in addition to the 2

mM thymidine at 30 h (Fig. 17, lanes 3 and 4 right). Whole cell lysates were prepared in 50 mM Tris-HCl pH 7.5, 150 mM NaCl, 50 mM NaF, 1% Tween-20, 0.5% NP40, and 1 x protease inhibitor mixture (Roche Applied Science, Indianapolis, IN) on ice for 30 min. Cleared cell lysates were resolved in 4-12% Bis-Tris gels (Invitrogen, Carlsbad, CA) and immunoblotted with anti-acetyl-Histone H4 primary antibody (Upstate Biotechnology, Lake Placid, NY) [33]. Increased histone acetylation was seen in both asynchronous and synchronized G1-phase populations of HeLa cells treated with TSA (Fig. 17, lanes 2 and 4, respectively). Cell blocks were generated using synchronized G1-phase populations of HeLa cells and 5  $\mu\text{m}$  sections were mounted onto a glass slide without any staining as described in Section 6.3.1.

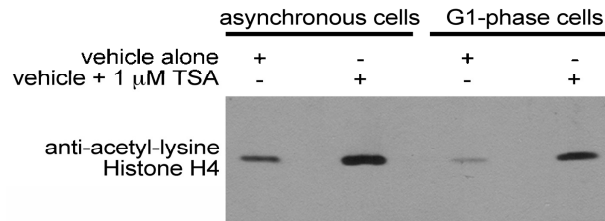


Fig. 17. Immunoblot of acetyl-Histone H4 in asynchronous and synchronized G1-phase HeLa cells treated with vehicle or TSA for 6 hours. Increased acetyl-Histone H4 associated with chromatin decondensation is seen in cells treated with TSA.

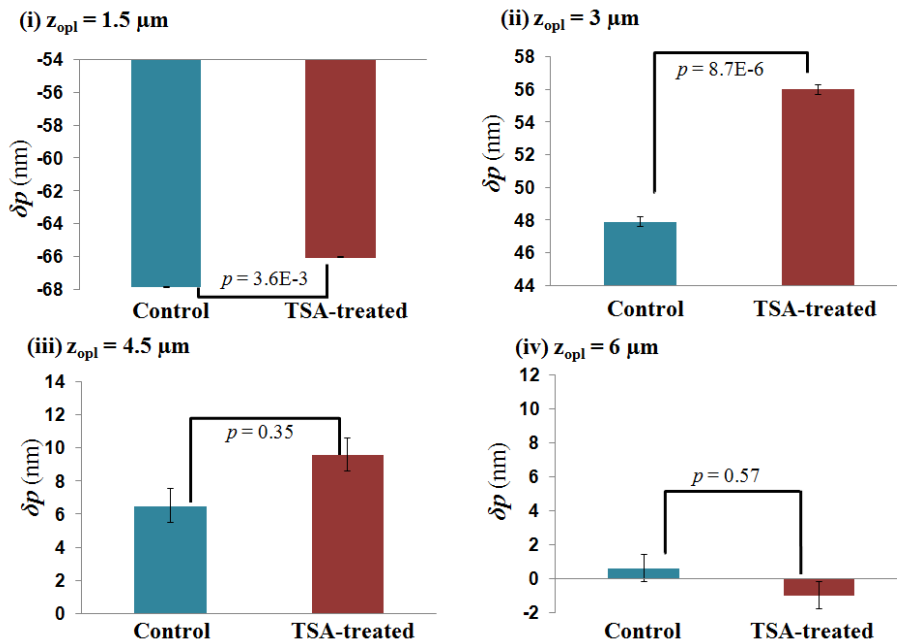


Fig. 18. The depth-resolved sub-resolution change in OPL ( $\delta p$ ) at four fixed optical-depth locations within the nuclei for control cells and TSA-treated cells.

The depth-resolved structural feature vector is extracted from about 70-75 cell nuclei of control and TSA-treated synchronized G1-phase populations of HeLa cells respectively.

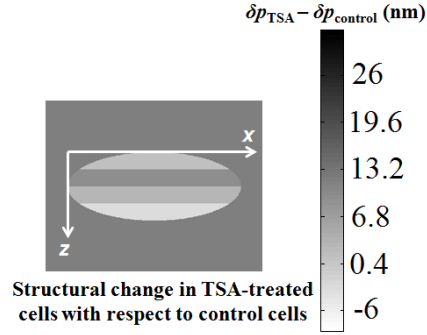


Fig. 19. The depth-resolved changes in nuclear structural feature vector distribution for the TSA-treated cells when compared to control cells.

Figure 18 shows the  $\delta p$  values, which quantify depth-resolved sub-resolution structural change in OPL, at four fixed optical-depth locations of  $1.5 \mu\text{m}$ ,  $3 \mu\text{m}$ ,  $4.5 \mu\text{m}$  and  $6 \mu\text{m}$  within the cell nucleus for the control and TSA-treated cells. The graphic visualization of the depth-resolved average nuclear structural feature vector changes, quantified by  $\delta(\delta p) = \delta p_{TSA} - \delta p_{control}$ , is shown in Fig. 19. A statistically significant increase in the average  $\delta p$  is observed at two optical depths ( $1.5$  and  $3 \mu\text{m}$ ) within cell nuclei for TSA-treated cells compared to the control cells, with the central location (one coherence length centered around  $3 \mu\text{m}$ ) exhibiting the most significant difference ( $P = 8.7E-6$ ). The nuclear density in control and TSA-treated cells is similar, as both cell groups are synchronized at  $G_1/S$  phase. As suggested by our simulation result (Fig. 9) in Section 5, the increased  $\delta p$  value in TSA-treated cells is attributed to chromatin decondensation and the increased correlation length [31] due to TSA-induced histone acetylation. The depth-resolved structural feature vector indeed captures such nanoscale chromatin conformational changes within the cell nucleus.

## 7. Conclusion

We have presented a novel yet simple approach that, given experimentally reasonable SNR levels, utilizes the coherence gating implicit in spectral-domain interferometry to generate a depth-resolved structural feature vector, which captures sub-resolution axial nanoscale structural changes at *fixed* sample optical depths that are at least one coherence length apart. Most importantly, we show that the depth-resolved structural feature vector is independent of sample thickness. Our approach is applicable to the analysis of depth-resolved nanoscale-sensitive structural characteristics directly on the clinically prepared unstained sample. We have demonstrated that the depth-resolved structural changes can provide insights into the structural transformation during the regulation of cell proliferation through cell cycle and chromatin decondensation induced by histone acetylation, and have the potential to be used as diagnostic markers for improving cancer diagnosis or characterizing the effect of pharmacological compounds.

## Acknowledgments

We thank Dr. M. A. Choma for valuable discussion on sub-resolution change in OPL in the early stages of this work.

This study was supported in part by National Cancer Institute (CA164433 and CA148644), the Broad Medical Research Program of The Broad Foundation, Magee-Women's Foundation, James F. Walsh Foundation and National Institute of Health through UL1RR024153 and UL1TR000005.